Research Report of Intelligent Systems for Medicine Laboratory
Report # ISML/02/2013, March 2013

Evaluation of accuracy of patient-specific non-linear biomechanical models used to predict intraoperative brain shift

Aditi Roy, Revanth Reddy Garlapati, Ahmed Mostayed

Intelligent Systems for Medicine Laboratory
The University of Western Australia
35 Stirling Highway
Crawley WA 6009, Australia
Email: aroy@mech.uwa.edu.au
Website: www.mech.uwa.edu.au/ISML

Abstract

Pre-operative brain images that are registered onto relevant intra-operative images can enhance neuronavigation during image-guided surgery. In this work, the accuracy of non-rigid registration results based on biomechanical modelling is compared with those of rigid registration for 33 cases of neurosurgery. Patient-specific biomechanical models were implemented using specialised non-linear finite element procedures in order to predict the deformation fields within the brain. The procedures utilise the Total Lagrangian formulation with explicit time stepping and dynamic relaxation. We used patient-specific finite element meshes consisting of hexahedral and non-locking tetrahedral elements, together with realistic material properties for the brain tissue and appropriate contact conditions at the boundaries. The loading was defined by prescribing deformations on the exposed brain surface in the craniotomy area. The computed deformation fields were used to warp the pre-operative images. An edge-based Hausdorff distance metric based on Canny edges was developed for evaluation of accuracy of registration results using the intraoperative images. Subsequently, a test for difference in proportions for the paired-sample design was conducted to test the hypothesis that the proportion of patients for whom improved neuronavigation can be achieved due to application of biomechanical model-based non-rigid registration is same as that of rigid registration. This hypothesis was rejected on the basis of results obtained from statistical analysis. The outcome of the analysis suggests that non-linear biomechanical models can be regarded as one possible method of improving neuronavigation.

Keywords: Brain shift, non-rigid registration, non-linear biomechanical models, Hausdorff distance

Contents

1. Introduction

Malignant glioma is the most common primary brain tumour in adults. It generally presents with epilepsy, cognitive change, headache, dysphasia, or progressive hemiparesis (Davies et al., 1996). Diagnosis is usually achieved by appropriate imaging studies followed by biopsy or neurosurgical resection (Thomas and Graham, 1980). Near-total surgical removal is desirable for delayed malignant progression (Berger et al., 2006, Berger and Rostomily, 1997, Keles et al., 2001, Nakamura et al., 2000, Piepmeier et al., 1996, Scerrati et al., 1996), decreased risk of seizures (Luyken et al., 2003), and prolonged survival. It is difficult to achieve due to the uncertainty in visual distinction of gliomatous tissue from adjacent healthy brain tissue. More complete tumour removal can be achieved through image-guided neurosurgery that uses intra-operative magnetic resonance images (MRIs) for improved visualization. The efficiency of intra-operative visualization and monitoring can be significantly improved by fusing high resolution pre-operative imaging data with the intra-operative configuration of the patient's brain. This can be achieved by updating the pre-operative image to the current intra-operative configuration of the brain through registration.

During neurosurgery, however, the brain deforms, up to 10 mm in some cases(Wittek et al., 2007). This deformation is due to several factors such as loss of cerebrospinal fluid (CSF), gravity, administered drugs, tissue resection and removal, intracranial pressure, etc. According to Nabavi and his colleagues (Hu et al., 2007) gravity alone can cause a very wide range of brain shift (0-50mm) throughout the course of neurosurgery (see Figure 1.1). It is believed that brain shift contributes to the inaccuracy of neuro-surgical navigation systems more than anything else (Skrinjar et al., 2001).

Intra-operative imaging is the most straight forward way to capture the brain deformation during surgery. Intra-operative MRI scanners are very expensive and often cumbersome. Hardware limitations of these scanners make it infeasible to achieve frequent whole brain imaging during surgery. As an alternative the pre-operative MRI can be updated to the current configuration of the operating room. The contemporary way to update the pre-operative image is to non-rigidly register it with the intra-operative image. However, this approach still requires frequent acquisition of the intra-operative images. An alternative

approach is to acquire very rapid sparse intra-operative data and predict the deformation for the whole brain.

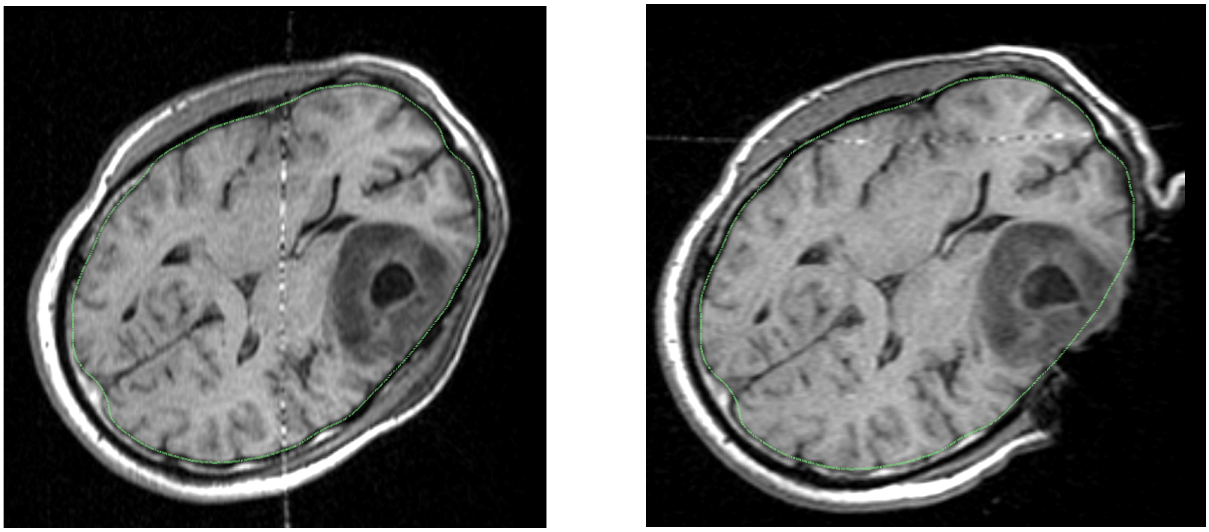

(1.1.a) (1.1.b)

Figure 1.1: An example of craniotomy induced brain shift. (a) pre-operative MRI and (b) intra-operative MRI. Contour of the pre-operative brain surface is shown in green

The Intelligent Systems for Medicine Laboratory in UWA has developed a suite of algorithms, for real time prediction of the brain deformation from sparse intra-operative data (Joldes et al., 2009d, Joldes et al., 2010). In our previous publications the accuracy of predicted brain shift was demonstrated with six craniotomy cases (Wittek et al., 2007, Joldes et al., 2009a). Recently we developed an edge-based Hausdorff distance measure (Garlapati et al., 2012) to evaluate the accuracy of registration quantitatively. The accuracy of registration results obtained from our algorithm and rigid registration (as implemented in ITK and 3D Slicer) were compared for five clinical cases. The results showed higher registration accuracy for our algorithm than the rigid registration. However, evaluation of registration result on a large number of clinical cases is required before our algorithm can be integrated in a commercially available neuro-navigation system.

This paper reports our initial effort to design a statistical hypothesis testing system to demonstrate the efficacy of our algorithms for image-guided neurosurgery on a large sample of neurosurgery images. In order to do so the alignment errors for biomechanics-based registration algorithm developed at ISML and the rigid registration were computed for thirty three neurosurgery cases. A criterion for successful registration was then defined based on the alignment error. Then a significance test for difference in success proportion (Connor, 1987)

was done to reject the null hypothesis that the proportion of patients for whom improved neuro-navigation can be achieved is same for both rigid and non-rigid registration. Our initial results with these thirty three cases are encouraging as a statistically significant difference in success proportion between the two algorithms was achieved. It leads us to believe that even for larger sample sizes our algorithm will perform significantly better.

2. Methods

33 Cases of neurosurgery were obtained from our collaborator's database (Computational Radiology Lab, Harvard Medical School), and in order to avoid selection bias, the cases were selected at random.

2.1 Patient-specific biomechanical model of brain

The generation of patient-specific biomechanical model of brain requires construction of the computational grid, assignment of mechanical properties, enforcing boundary conditions and loading.

2.1.1 Computational grid generation

A three dimensional (3D) surface model of each patient's brain was created from segmented pre-operative magnetic resonance image (MRI). The parenchyma, ventricles and tumour was segmented using 3D slicer (www.slicer.org) (Slicer).

The meshes were constructed using low-order elements (linear tetrahedron or hexahedron) to meet the computation time requirement. In general hexahedral elements are preferred to model behaviour of almost incompressible continua like brain. Linear tetrahedral elements are not used to avoid volumetric locking (Bathe, 1996). Although fast and accurate algorithms are available for automatic generation of tetrahedral meshes(Viceconti et al., 2004), only few template-based algorithms are available for meshing using hexahedra (Owen, 2001, Viceconti and Taddei, 2003) . However, template-based algorithms cannot be used to mesh tumours due to the unpredictable nature of tumour growth. Therefore, mixed meshes

having both hexahedral and tetrahedral elements (predominantly hexahedra) were used to automate the mesh generation process. To prevent volumetric locking the tetrahedral elements with average nodal pressure (ANP) formulation (Joldes et al., 2009c) was used. In addition an efficient hourglass control mechanism was built for the hexahedral elements in order to eliminate the instabilities known as zero-energy mode (Joldes et al., 2008a). The meshes were generated using IA-FEMesh (Grosland et al., 2009) and Hypermesh (commercial FE mesh generator by Altair of Troy, MI, USA). An example of the brain mesh is shown in Fig 2.1.

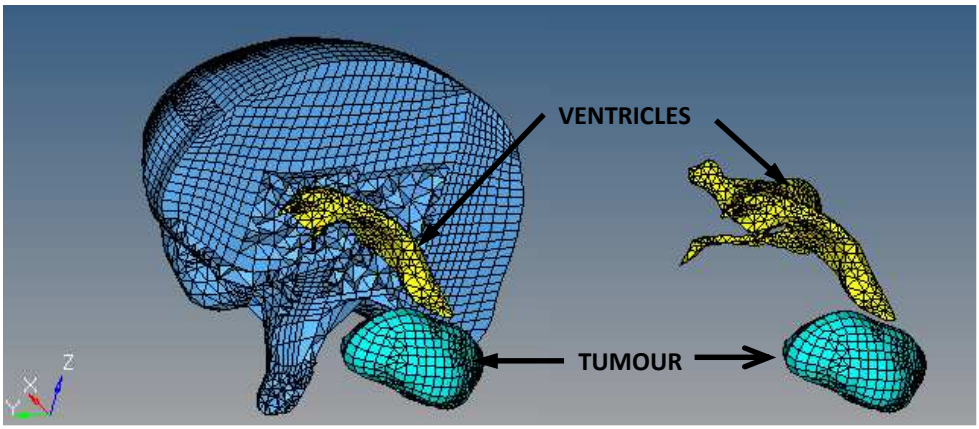

Figure 2.1: An example of patient -specific brain mesh (case no 07; no of elements 99974 and no of nodes 32023).

2.1.2 Displacement loading

There are always uncertainties regarding the patient-specific properties of the living tissues. In order to lessen the effects of such uncertainties, the models were loaded by prescribing displacements on the exposed part of the brain surface (Figure 2.2). For this type of loading the unknown deformation field within the brain depends very weakly on the mechanical properties of the brain tissues (Wittek et al., 2009).

At first the pre-operative and intra-operative coordinate systems were aligned by rigid registration. Then the displacements at the mesh nodes located in the craniotomy region (see Figure 2.3) were determined by B-spline non-rigid surface registration of the intra-operative and pre-operative brain surface.

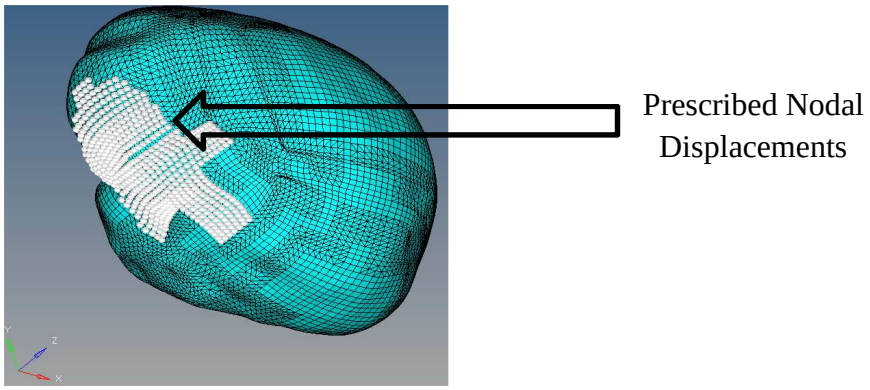

Figure 2.2: Model loading through prescribed nodal displacements at the exposed brain surface

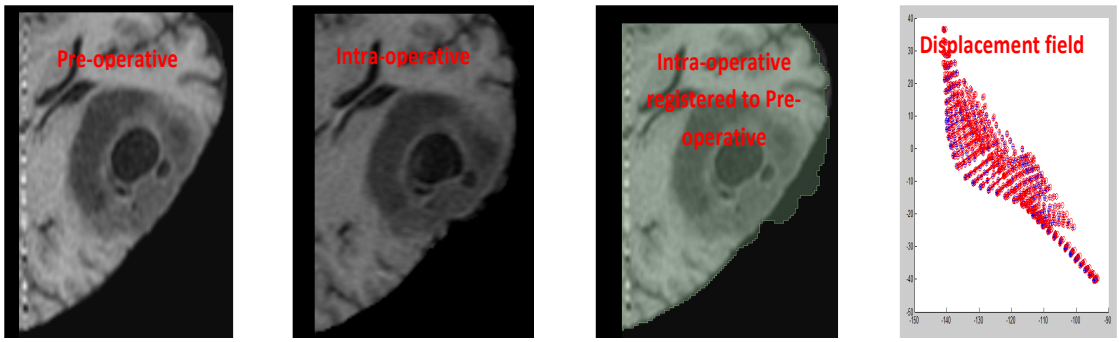

Figure 2.3: Determining displacement field

2.1.3. Boundary conditions

During craniotomy cerebral fluid (CSF) can leak from the subarachnoid space and create a gap between brain and skull. The stiffness of the skull is several orders of magnitude higher than that of the brain tissue. Therefore, in order to define the boundary conditions for the unexposed nodes of the brain mesh, a contact interface (Joldes et al., 2008b) was defined between the rigid skull model and the deformable brain (Figure 2.4). The interaction was formulated as a finite sliding, frictionless contact between brain and skull. This contact formulation prevents the brain surface form penetrating the skull by checking the nodes of the brain mesh for penetration (Joldes et al., 2008b).

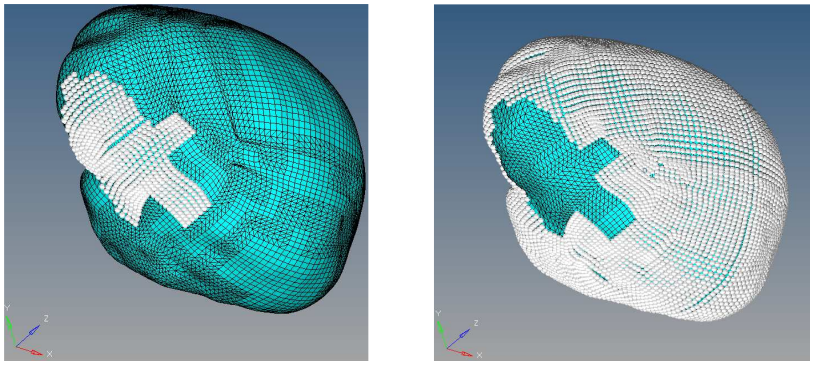

Figure 2.4: The nodes where boundary and contact conditions are applied

Load nodes and contact nodes

2.1.4 Mechanical properties of the intracranial constituents

Despite continuous efforts (Sinkus et al., 2005, Miller and Chinzei, 2002), commonly accepted non-invasive methods for determining patient-specific constitutive properties of the brain and other soft organs' tissues have not been developed yet. Constitutive models of the brain tissue applied for computing the brain deformation for non-rigid registration vary from simple linear-elastic model (Warfield et al., 2000) to Ogden-type hyperviscoelasticity (Miller and Chinzei, 1997, Wittek et al., 2007) and bi-phasic models relying on consolidation theory (Miga et al., 2001). However the strength of the modelling approach used in this study is that the calculated brain deformations depend very weakly on the constitutive model and mechanical properties of the brain tissues. The neo-Hookean constitutive model (Yeoh, 1993) is used for the brain parenchyma and tumour as it has been indicated in the literature (Miller and Chinzei, 1997) that hyperelastic constitutive models are the best to represent the steady state behaviour of the brain tissue. Based on the experimental data by Miller and Chinzei (Miller and Chinzei, 2002), Young's modulus of 3000 Pa was selected for the parenchyma. The Young's modulus for tumour was assigned two times larger than for parenchyma, keeping it consistent with the experimental data of (Sinkus et al., 2005). As the brain tissue is almost incompressible, Poisson's ratio 0.49 was chosen for the parenchyma and tumour following (Wittek et al., 2007). Following (Wittek et al., 2007) the ventricles were assigned properties of very soft compressible elastic solid with Young's modulus of 10 Pa and Poisson's ratio of 0.1. Density 1000kg/m3 was chosen for parenchyma and tumour and ventricles.

The material properties are summarised in table2:

Table 2: Summary of the material properties used for the brain mesh

	Young's modulus (Pa)	Poisson's ratio	Density (kg/m^3)
Brain Parenchyma	3000	0.49	1000
Tumour	6000	0.49	1000
Ventricles	10	0.10	1000

2.1.4 Algorithms for integration of equations of solid mechanics

An efficient algorithm for integrating the equations of solid mechanics has been developed by (Miller et al., 2007). The computational efficiency of this algorithm is achieved by using - 1) Total Lagrangian (TL) formulation(Miller et al., 2007) for updating the calculated variables; and 2) Explicit Integration in the time domain combined with mass proportional damping. In the TL formulation, all the calculated variables (such as displacements and strains) are referred to the original configuration of the analysed continuum (Joldes et al., 2009b). The decisive advantage of this formulation is that all derivatives with respect to spatial coordinates can be pre-computed which greatly reduces the computation time in comparison to Updated Lagrangian formulation used in vast majority of commercial finite element solvers such as LSDYNA, ABAQUS (Miller et al., 2007). The Total Lagrangian formulation also leads to a simplification of material law implementation as these material models can be easily described using the deformation gradient (Joldes et al., 2009d).

In addition to that application of the Total Lagrangian formulation simplifies the material law implementation since the hyperelastic material models, such as the neo-Hookean model used here for the brain parenchyma and tumour, can be easily described using the deformation gradient. In explicit time integration, the central difference method is applied in this study where the displacement at time $t+\Delta t$ (Δt is the time step) is solely based on the equilibrium at time t. This makes the treatment of nonlinearities very straightforward and no iterations are required. By using a lumped (diagonal) mass matrix, the equations of motion can be

decoupled and no system of equations is needed to be solved. Computations are done at the element level eliminating the need for assembling the stiffness matrix of the entire model. As a result application of explicit integration can reduce by an order of magnitude the time required to compute the brain deformations in comparison to implicit integration typically used in commercial finite element codes (such as e.g. LS-DYNA, ABAQUS) for steady state solutions(Wittek et al., 2010). Combining the explicit integration in time domain with mass proportional damping provides further increase in the computational efficiency when reaching the steady state solution without compromising the solution accuracy (Joldes et al., 2009d).

These algorithms are also implemented in GPU (NVIDIA Tesla C1060 installed on a PC with Intel Core2 Quad CPU) for real time computation so that the entire model solution takes less than four seconds on a commodity hardware (Joldes et al., 2010).

2.2. Evaluation of registration accuracy

The accuracy of image registration is assessed by evaluating the registered pre-operative image using intra-operative image as ground truth. There is no universally accepted “gold standard” for validation of image registration techniques yet (Chakravarty et al., 2008). Although similarity metrics such as mutual information and correlation ratio are available for rapid and automatic evaluation of image registration, they do not provide the alignment error in terms of Euclidean distance (Rexilius et al., 2001). Therefore, validation of image registration has been often done using comparison between landmarks that were manually selected by experts in the respective MRIs(Ferrant et al., 2002, Hu et al., 2007). Though the interpretation of the results of landmarks-based validation is straightforward, determining the position of landmarks relies on the experience of an expert (Miga et al., 1999).

Hausdorff Distance is a similarity metric that can compute registration error in an objective, automatic and fast manner. In a recent study of our research group, the ventricles were segmented from the registered pre-operative image and the intra-operative image, and the point sets representing the surfaces of both these segmentations were compared using a point-based Hausdorff Distance metric(Wittek et al., 2010). Such methods are time consuming, labour-intensive and subjective to human errors (Fedorov et al., 2008). To overcome these

short comings an objective evaluation method based on canny edges(Canny, 1986) of two dimensional images in the axial and sagittal planes was developed recently (Garlapati et al., 2012). In this study, edge-based Hausdorff Distance metric was used in evaluation of image registration accuracy.

Hausdorff distance is a popular measure to calculate similarities between images (Huttenlocher et al., 1993). The Hausdorff distance is used to compare two sets of feature points. According to traditional point-based Hausdorff distance, if $A = \{a_1, \dots a_n\}$ and $B = \{b_1, \dots b_n\}$ are two feature point sets that include points corresponding to the non-zero pixels on the canny edge images, then the directed distance between them $h(A, B)$ is defined as the maximum distance from any of the points in the first set to the second one and can be defined as follows:

$$h(A, B) = argmax_{a \in A}[argmin_{b \in B}||a - b||_2] \quad (1)$$

$$h(B, A) = argmax_{b \in B}[argmin_{a \in A}||b - a||_2] \quad (2)$$

The Hausdorff distance, HD between two points A and B is $H(A, B)$ which is the maximum of the two directed distances and is defined as follows

$$H(A, B) = \max(h(A, B), h(B, A)) \quad (3)$$

In order to remove outliers the percentile Hausdorff distance is proposed with some modification (Zhao et al., 2005) and the directed distance is defined as follows:

$$h_p(A, B) = P^{th}{}_{a \in A}[argmin_{b \in B}||a - b||_2] \quad (4)$$

Where P is P^{th}percentile of $[argmin_{b \in B}||a - b||_2]$

In order to measure misalignments between two medical images the distance between local features in two images such as MRI contour lines of brain tumour can be used. In order to do so, edge-based Hausdorff distance is proposed. In this case directed distance between two sets of edges is defined as follows:

$$h_e(A^e, B^e) = argmax_{a_i^e \in A^e}[argmin_{b_j^e \in B^e} \left|\left|a_i^e - b_j^e\right|\right|] \quad (5)$$

Where $A^e = \{a_1^e, \dots a_m^e\}$ and $B^e = \{b_1^e, \dots b_m^e\}$ are two sets of edges.

The quantity $\left|\left|a_i^e - b_j^e\right|\right|$ in Eq. 5 is the point-based Hausdorff distance between two point sets M= $\{m_1, \dots m_p\}$ and T= $\{t_1, \dots t_p\}$ representing edges a_1^e and b_1^e respectively. The edge-based Hausdorff Distance is then defined as follows

$$H_e(A^e, B^e) = \max(h_e(A^e, B^e), h_e(B^e, A^e)) \quad (6)$$

Similar to the percentile point-based Hausdorff distance, the percentile edge-based Hausdorff distance can be constructed as follows:

$$h_{pe}(A^e, B^e) = P^{th}{}_{a_i^e \in A^e}[argmin_{b_j^e \in B^e}||a_i^e - b_j^e||] \quad (7)$$

This percentile edge-based Hausdorff distance is useful in two ways: it can enable identification of potential outlier edge pairs and can report Hausdorff distance values for different percentiles (Mostayed et al., 2013) .

In this method, the edges shorter than 5 mm are deleted from the images, as in comparison to brain dimension (approximately 150 mm), this dimension is insignificant. The edges are made consistent with respect to each other using the round-trip threshold procedure as described in our previous paper (Garlapati et al., 2012). The purpose of this is to remove features that have no correspondence. The round-trip threshold in this study is set to 2 mm.

The three dimensional (3D) MRI images, being compared, were cropped only to include region of interest (ROI) enclosing the tumour and the craniotomy area. Subsequently, a single two dimensional (2D) representative image was obtained from these 3D images in both axial and coronal planes. The edge-based HD metric is used to evaluate the non-rigid registration accuracy by comparing each warped pre-operative 2D image with the corresponding intra-operative image. Similarly, for rigid registration, pre-operative images are compared with corresponding intra-operative images. The original image resolution of the images are 0.938 × 0.938 × 2.5 mm^3 (all the cases except case-07,case-16 and case-33) or 0.859 × 0.859 × 2.5 mm^3 (case-07,case-16 and case-33); whereas to increase precision of Canny edges in

axial/coronal 2D images the original 3D images are resampled to a resolution of 0.5×0.5×0.5 mm^3.

Most of the edges used for HD computation have a corresponding edge in the other image. Some of the Canny edges in the images do not represent the same anatomical feature, and therefore lack correspondence. The presence of such pairs leads to unusually large values of

edge-based HD metric values—these are considered outliers, and excluded from the final HD analysis, as they do not indicate registration accuracy correctly. These outliers are identified from the slices under observation.

2.3 Statistical analysis

In order to make reliable decisions in medical research, appropriate and adequate statistical analysis is necessary (Cadarso-Suárez and González-Manteiga, 2007). To demonstrate the validity of conclusions of this work we need to design and apply an appropriate hypothesis test. A hypothesis test involves two opposing hypotheses: a null hypothesis denoted by H_0 and alternative hypothesis denoted by H_a. In order to determine whether there is enough evidence from the sample to reject H_0 we calculate P-value. Then we compare the computed P-value that is probability of rejecting the null hypothesis of a study when in fact the hypothesis is true with α level of significance. For any value of α, if P-value is less than α, H_0 can be rejected. A value of 0.05 is often used for α. The smaller the P-value, the stronger the weight of evidence favouring the rejection of H_0.

2.3.1 P-value calculation

P-value is the estimated probability of rejecting the null hypothesis of a study when in fact the hypothesis is true (Goodman, 1999). It indicates the extent to which the sample evidence supports the decision to reject H_0.

P-value = probability of observing a value of the test statistics as extreme or more extreme than the observed statistic calculated from samples, given H_0 is true (Shaffer, 1995).

Considering Ω_1 and Ω_2 are two distinct populations and $p_1 - p_2$ is the difference between proportions in each population to be studied is equal, the difference in sample proportions $\overline{p_1} - \overline{p_2}$ from large independent random samples of sizes n_1 from Ω_1 and sizes n_2 from Ω_2 Then

$$\overline{p_1} = \frac{x_1}{n_1} \tag{8}$$

and

$$\overline{p_2} = \frac{x_2}{n_2} \tag{9}$$

Where x_1 and x_2 are the number of "YES" responses (false null hypothesis) in the respective samples. Under the assumptions that the true proportions are equal

Pooled sample proportion $\hat{p} = \frac{x_1 + x_2}{n_1 + n_2}$ (10)

Pooled sample proportion is the proportion of the total number of "YES" responses from both samples combined. Using the value of the pooled sample proportion the standard error can be calculated as follows

$$SE = sqrt\{\hat{p} * (1 - \hat{p}) * [\left(\frac{1}{n_1}\right) + \left(\frac{1}{n_2}\right)]\} \tag{11}$$

The test statistics is a Z score (Z) defined by the following equation

$$Z = \frac{\overline{p_1} - \overline{p_2}}{SE} \tag{12}$$

On the other hand, when $p_1 - p_2$, the difference between proportions in each population to be studied, is equal to some fixed value other than zero, and is equal to δ then

$$Z = \frac{(\overline{p_1} - \overline{p_1}) - \delta}{SE} \tag{13}$$

The test statistic is Z score and, the P-value associated with this score can be calculated from the normal distribution curve or calculator.

2.3.2 Computation of P-value of the test for difference in proportions

In order to compare biomechanical model-based registration method with rigid registration of pre-operative and intra-operative MRI's, which is a standard method currently available to patients (Warfield et al., 2005, Jolesz et al., 2002) P-value, which is used to test for difference in proportions of the paired-sample design (Connor, 1987) is performed.

The null hypothesis is as follows:

Hypothesis (to be rejected by the proposed study): there will be no statistically significant increase in the proportion of neurosurgery patients for whom accurate data for intraoperative navigation is obtained, when using our biomechanics-based method as compared to rigid registration.

To reject the hypothesis, P-value is calculated both for zero and non-zero values of delta (difference in proportions that we would like to detect). The success criterion for the test is based on

1. Edges registered successfully: The percentile-HD metric value curve provides the percentage of edges successfully registered. The edge detection accuracy is limited to image resolution. The alignment error less than two times the in-plane resolution of intra-operative image is considered acceptable. For cases analysed here, have different image resolution. For cases- 07, case-16 and case-33, the in plane image resolution is 0.859 and thus the acceptable alignment error should be less than or equal to 2*0.859 which is 1.7 mm. Edge pair having HD value less than 1.7 mm was considered as successfully registered for these cases. For the remaining cases the image resolution is 0.938 and thus the edges having HD metric value less than 2*0.938 or 1.9 mm was considered as successfully registered.

2. The HD metric values at higher percentiles, which indicate the extent of misalignment in edges that have not been successfully registered. It is useful to consider the 100, 95 and 75-percentile HD metric values for this purpose. It is

important to note that the obvious outliers, i.e., the edges with no correspondence have been removed from the percentile-HD metric analysis. The secondary criterion is especially useful, when both rigid and non-rigid registration have approximately the same percentage of successfully registered edges.

3. Results

The prescribed displacement loading that was to be applied on the patient-specific biomechanical models was categorised on the basis of magnitude of corresponding displacements in table 3.1:

Table 3.1: Percentile analysis of magnitude of prescribed loading for various neurosurgery cases

Case No	100-Percentile-Displacement Loading (mm)	**90-Percentile Displacement Loading (mm)**	75-Percentile Displacement Loading (mm)	50-Percentile Displacements Loading (mm)	Comments about deformation
01	5.01	**3.12**	2.32	1.65	Large
02	6.01	**5.13**	4.49	2.71	Large
03	3.66	**2.01**	1.55	1.06	Small
04	6.07	**4.98**	2.82	1.96	Large
05	5.62	**3.42**	2.67	1.85	Large
06	4.15	**2.51**	1.57	0.95	Small
07	9.87	**6.47**	2.77	0.85	Large
08	7.30	**4.42**	2.12	1.40	Large
09	3.98	**2.70**	2.17	1.46	Large

10	4.43	**3.21**	1.92	1.01	Large
11	5.21	**3.21**	2.31	1.46	Large
12	8.92	**5.37**	2.84	1.46	Large
13	2.59	**2.01**	1.63	0.94	Small
14	9.36	**7.53**	5.70	2.60	Large
15	3.11	**2.18**	1.80	1.27	Small
16	5.77	**4.03**	2.26	0.98	Large
17	3.00	**2.35**	1.81	1.17	Small
18	4.23	**2.52**	1.85	1.38	Small
19	9.07	**5.69**	3.19	2.14	Large
20	5.08	**2.65**	1.76	0.78	Small
21	3.22	**2.44**	1.58	1.20	Small
22	3.21	**2.43**	1.93	1.25	Small
23	2.78	**2.41**	1.83	1.19	Small
24	1.16	**0.71**	0.62	0.45	Small
25	3.21	**2.34**	1.73	1.08	Small
26	5.37	**1.58**	1.10	0.66	Small
27	0.74	**0.64**	0.50	0.32	Small
28	4.87	**3.24**	1.96	1.54	Small
29	4.48	**3.29**	2.14	1.22	Small
30	2.28	**1.53**	1.24	0.97	Small
31	2.05	**1.30**	0.92	0.64	Small

32	3.81	**2.39**	1.80	1.46	Small
33	4.28	**3.94**	3.50	2.86	Large

From table 3.1, it is clear that 14 cases have considerably high deformation, and the remaining 19 cases have small deformation. Case 32 and case 33 were analysed in a previous study using different evaluation method (Wittek et al., 2010).

For all large deformation cases and one small deformation case (case-03), a qualitative comparison between the contours of warped pre-operative, pre-operative and intra-operative surfaces, overlaid on intra-operative images, was carried out at the exposed surface of the brain as shown in the figures 3.1, in both axial and coronal planes.

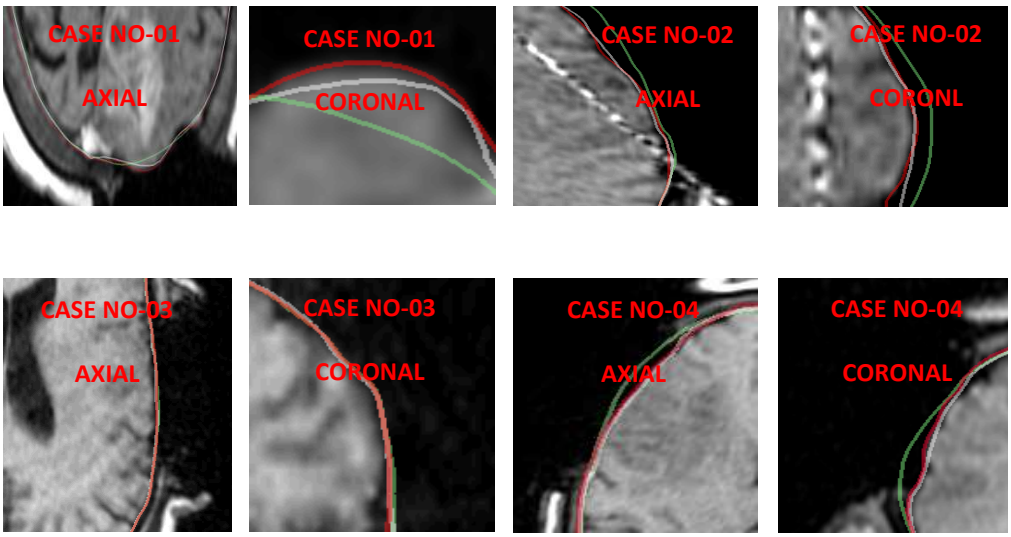

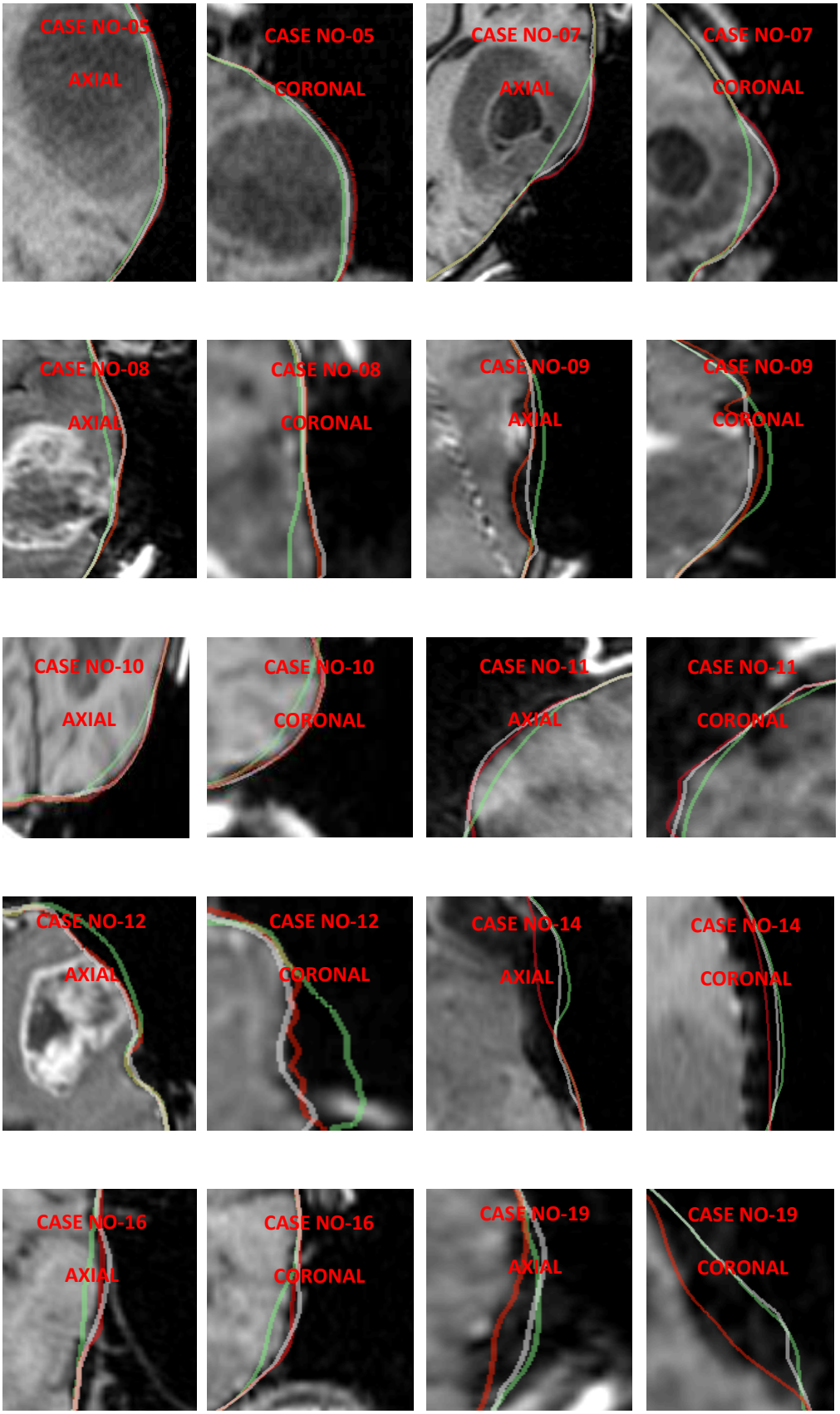
CASE NO-05
AXIAL
CASE NO-05
CORONAL
CASE NO-07
AXIAL
CASE NO-07
CORONAL
CASE NO-08
AXIAL
CASE NO-08
CORONAL
CASE NO-09
AXIAL
CASE NO-09
CORONAL
CASE NO-10
AXIAL
CASE NO-10
CORONAL
CASE NO-11
AXIAL
CASE NO-11
CORONAL
CASE NO-12
AXIAL
CASE NO-12
CORONAL
CASE NO-14
AXIAL
CASE NO-14
CORONAL
CASE NO-16
AXIAL
CASE NO-16
CORONAL
CASE NO-19
AXIAL
CASE NO-19
CORONAL

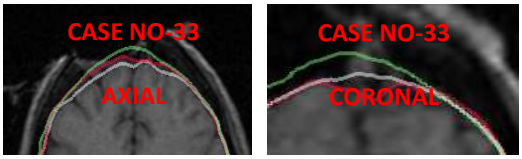

Figure 3.1: Contours of warped pre-operative, pre-operative and intra-operative images overlaid on intra-operative images (Green line is for pre-operative surface, red line is for intra-operative surface and white line is for warped pre-operative surface)

For 14 larges deformation cases, comparison between contours shows that the difference between warped pre-operative and intra-operative surfaces is less than that of pre-operative and intra-operative surfaces. On the other hand, all three contours are very close and almost similar in case of the one small deformation case.

Registration accuracy for these 15 cases of craniotomy-induced brain-shift was analysed by comparing the 2D Canny edges of representative images of warped pre-operative images with the corresponding intra-operative images using edge-based HD metric, in both axial and coronal planes. The overlaid Canny edges for non-rigid and rigid registration accuracy evaluation, are shown in figure 3.2.

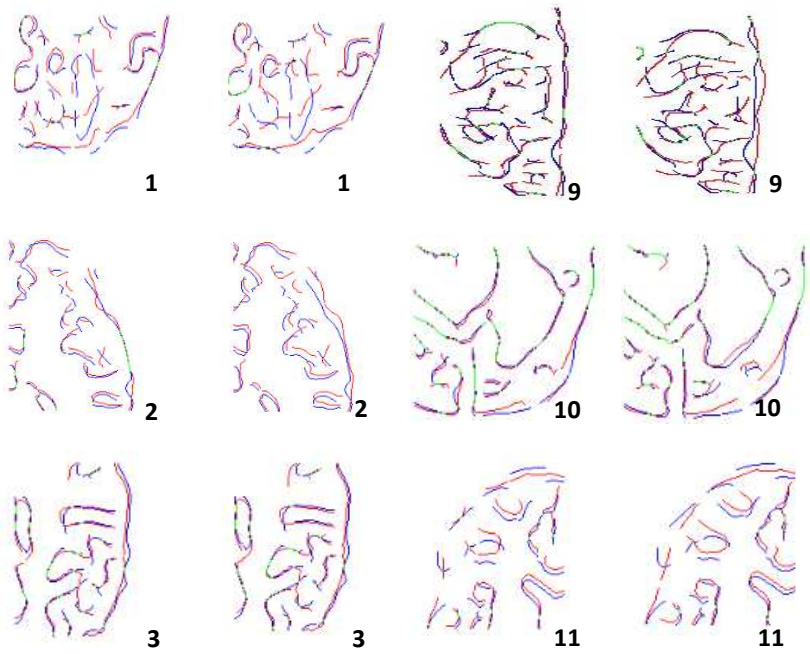

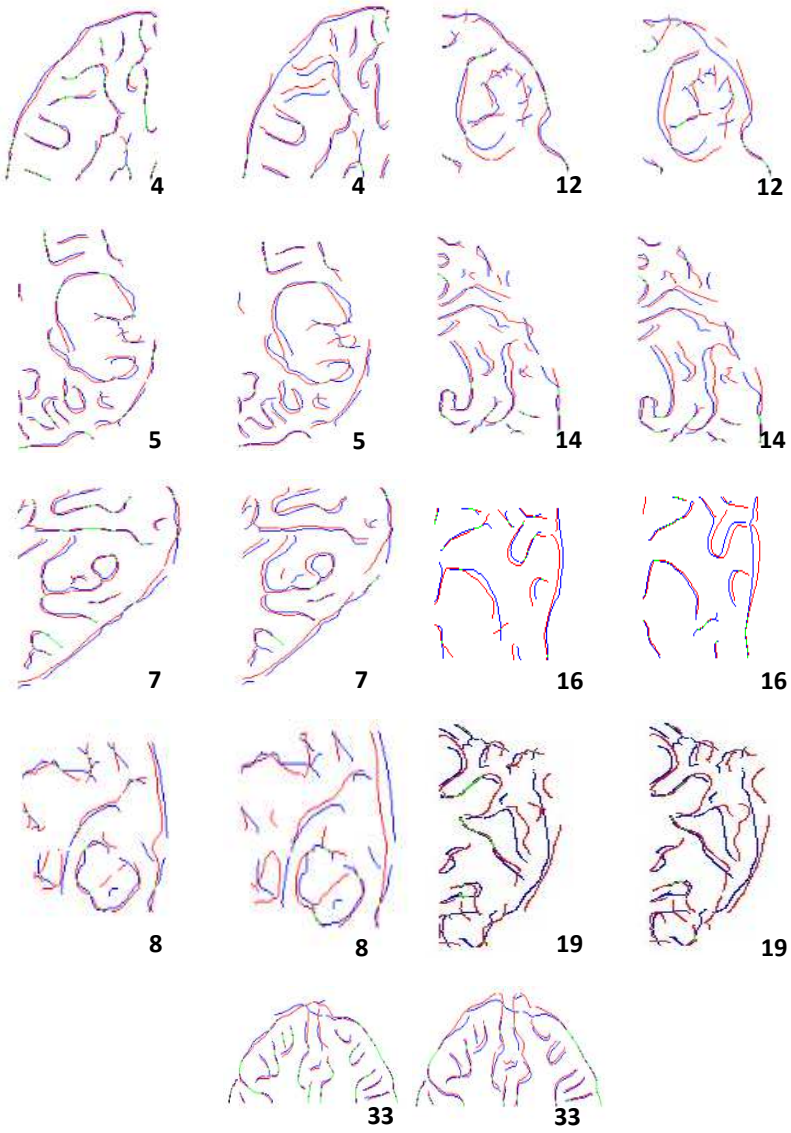

Figure 3.2: Overlaid Canny edges for non-rigid (left) and rigid registration (right) accuracy evaluation, in axial plane (the number on each image denotes a particular case). The green portion represents overlapping edges, the blue part identifies non-overlapping edges of the deformed pre-operative image and the red part identifies non-overlapping edges of the intra-operative image. The number on each image denotes a particular neurosurgery case.

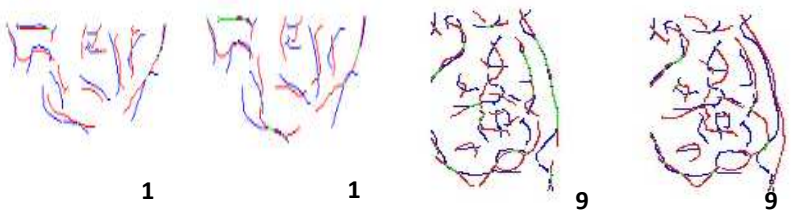

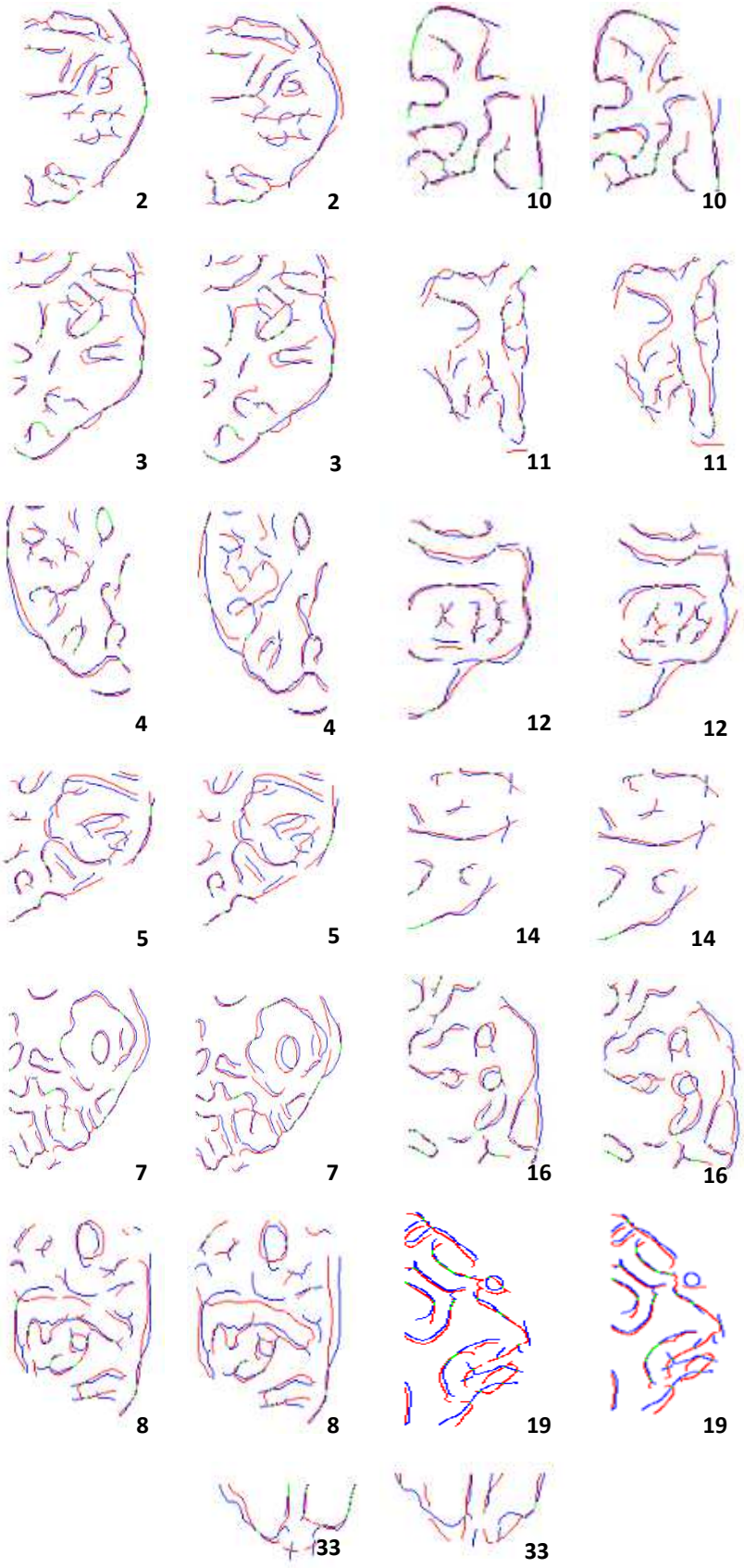

Figure 3.3: Overlaid Canny edges for non-rigid (left) and rigid registration (right) accuracy evaluation, in coronal plane (the number on each image denotes a particular case). The green

portion represents overlapping edges, the blue part identifies non-overlapping edges of the deformed pre-operative image and the red part identifies non-overlapping edges of the intra-operative image. The number on each image denotes a particular neurosurgery case.

Overlaid Canny edge images are qualitative indicators of the degree of misalignment between the images being compared. It was observed from the overlaid Canny edge images that the misalignments between the intra-operative and warped pre-operative images are less in comparison to those between the pre-operative and intra-operative images for all cases with considerably high craniotomy–induced deformations.

Registration accuracy of both non-rigid and rigid registrations, for the 15 cases was computed in axial and coronal planes, and the results are show in figure 3.4. The percentile-HD metric values for non-rigid and rigid registrations were plotted together in order to compare them with ease.

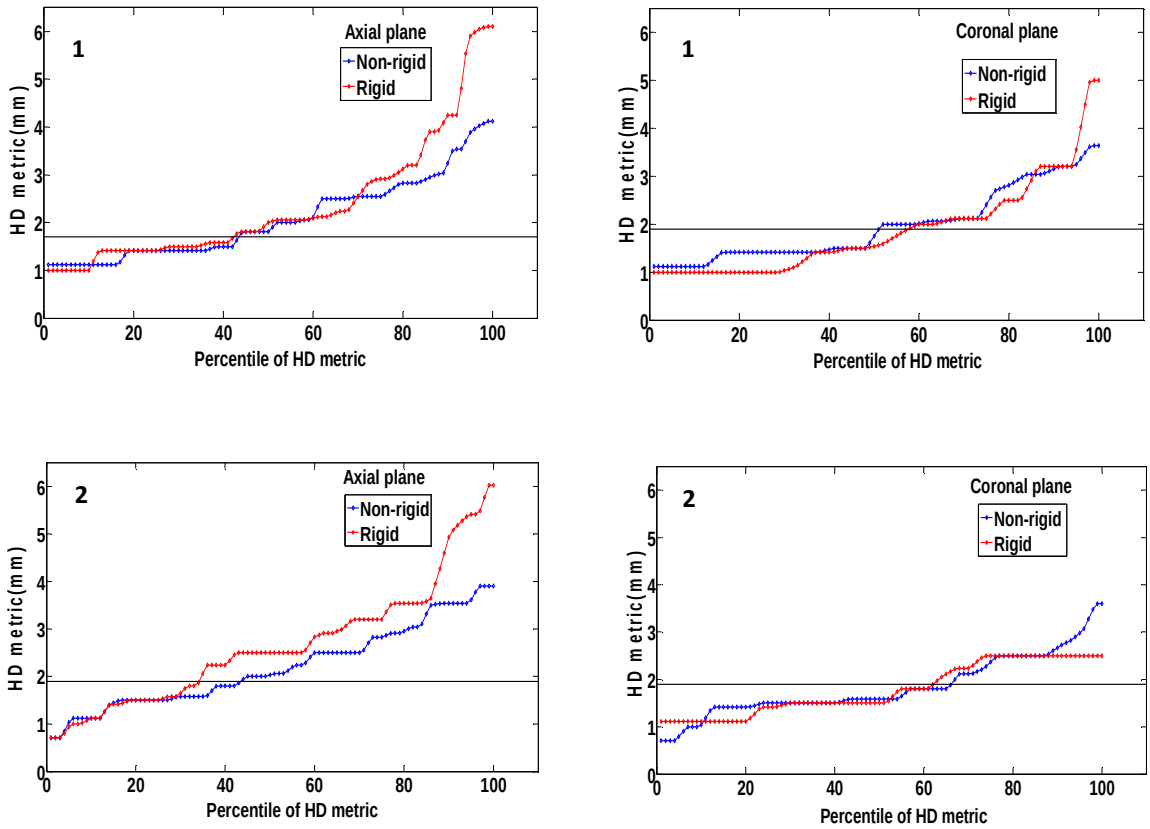

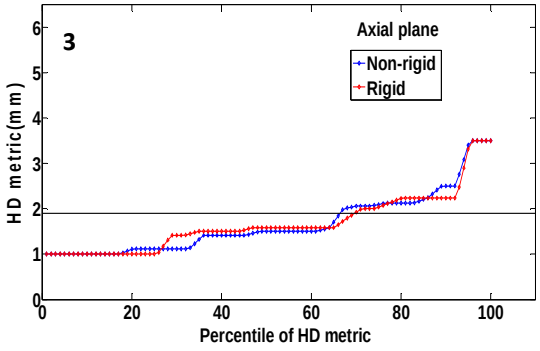
3
Axial plane
Non-rigid
Rigid
HD metric(mm)
Percentile of HD metric

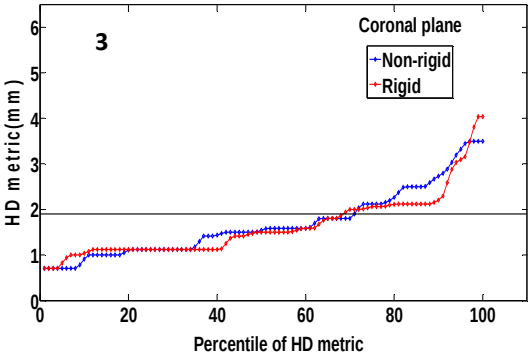
3
Coronal plane
Non-rigid
Rigid
HD metric(mm)
Percentile of HD metric

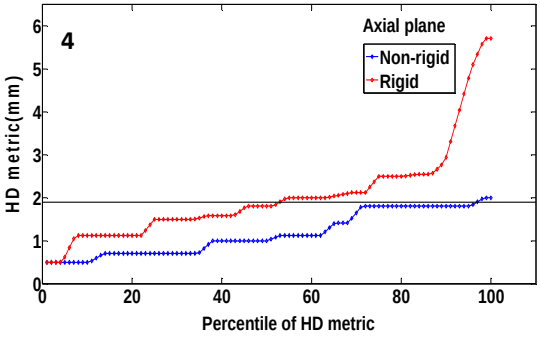
4
Axial plane
Non-rigid
Rigid
HD metric(mm)
Percentile of HD metric

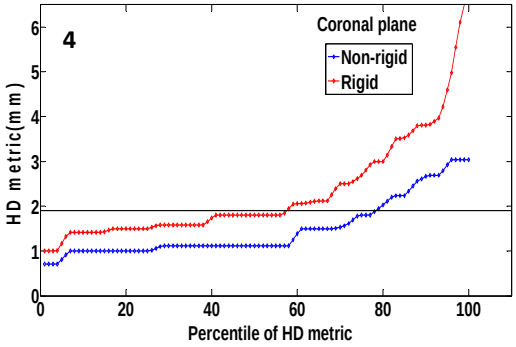
4
Coronal plane
Non-rigid
Rigid
HD metric(mm)
Percentile of HD metric

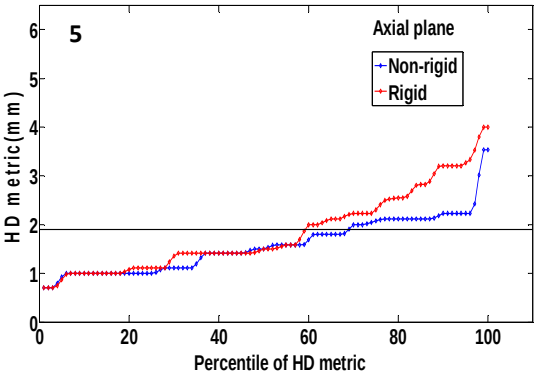
5
Axial plane
Non-rigid
Rigid
HD metric(mm)
Percentile of HD metric

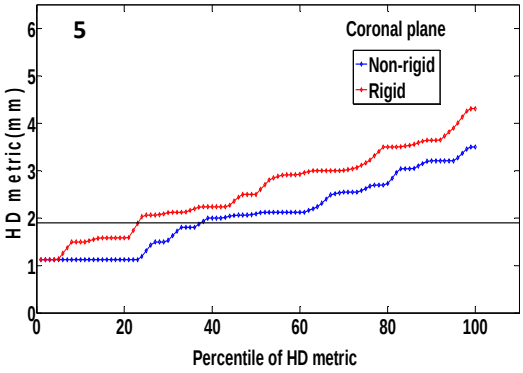
5
Coronal plane
Non-rigid
Rigid
HD metric(mm)
Percentile of HD metric

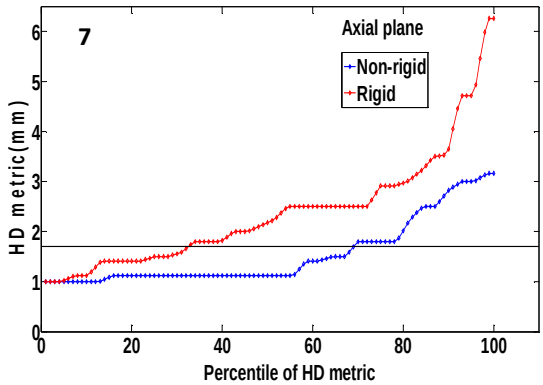
7
Axial plane
Non-rigid
Rigid
HD metric(mm)
Percentile of HD metric

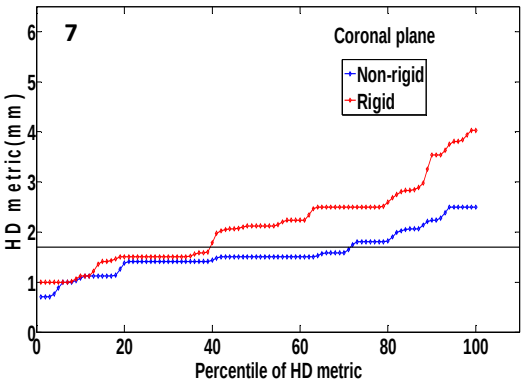
7
Coronal plane
Non-rigid
Rigid
HD metric(mm)
Percentile of HD metric

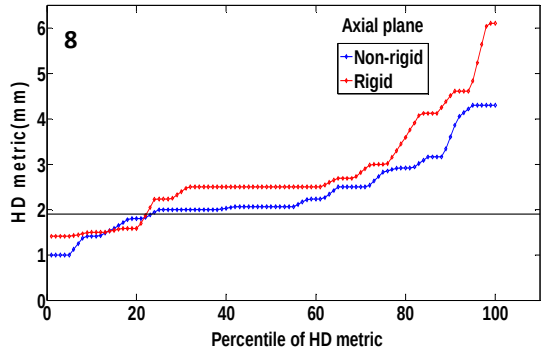
8
Axial plane
Non-rigid
Rigid
HD metric(mm)
Percentile of HD metric

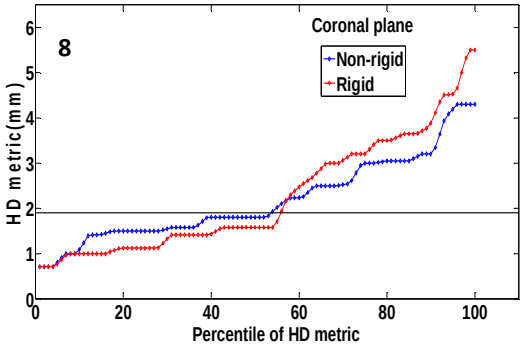
8
Coronal plane
Non-rigid
Rigid
HD metric(mm)
Percentile of HD metric

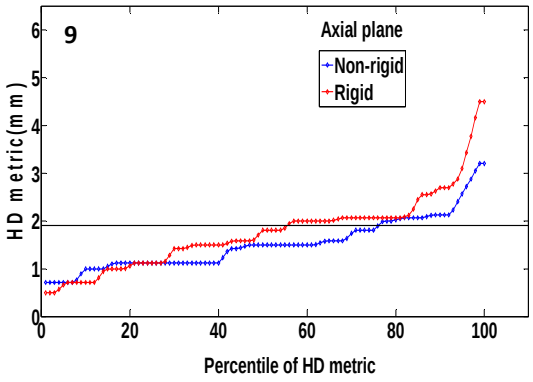
9
Axial plane
Non-rigid
Rigid
HD metric(mm)
Percentile of HD metric

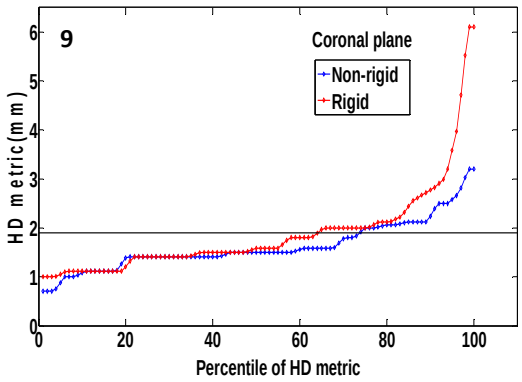
9
Coronal plane
Non-rigid
Rigid
HD metric(mm)
Percentile of HD metric

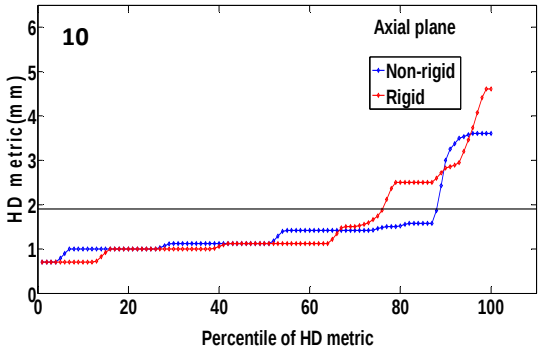
10
Axial plane
Non-rigid
Rigid
HD metric(mm)
Percentile of HD metric

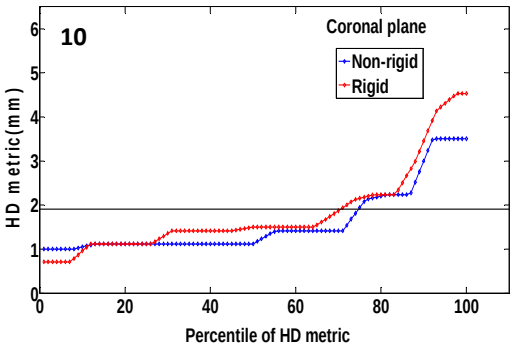
10
Coronal plane
Non-rigid
Rigid
HD metric(mm)
Percentile of HD metric

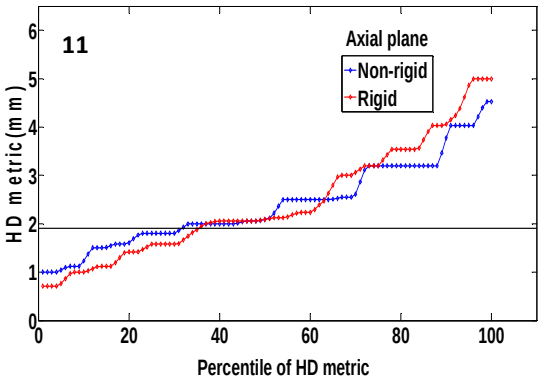
11
Axial plane
Non-rigid
Rigid
HD metric(mm)
Percentile of HD metric

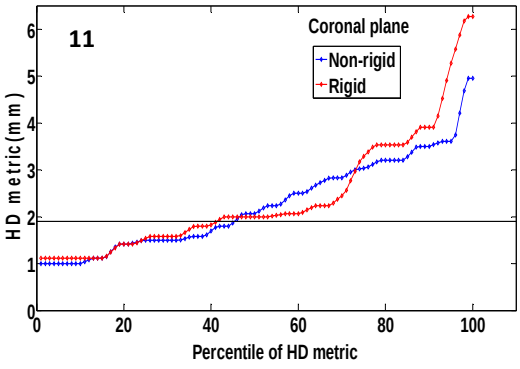
11
Coronal plane
Non-rigid
Rigid
HD metric(mm)
Percentile of HD metric

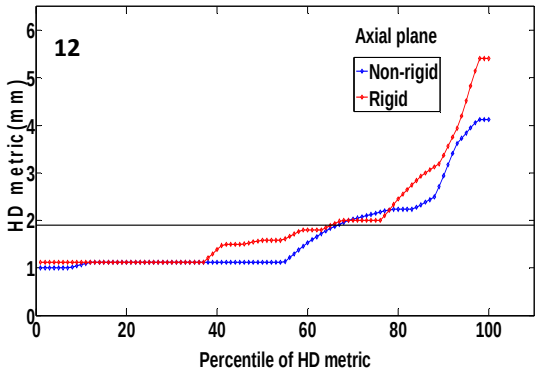
12
Axial plane
Non-rigid
Rigid
HD metric(mm)
Percentile of HD metric

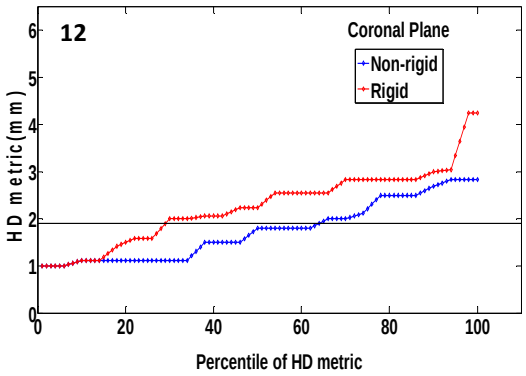
12
Coronal Plane
Non-rigid
Rigid
HD metric(mm)
Percentile of HD metric

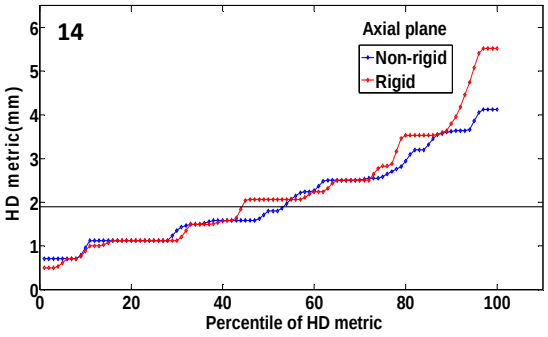
14
Axial plane
Non-rigid
Rigid
HD metric(mm)
Percentile of HD metric

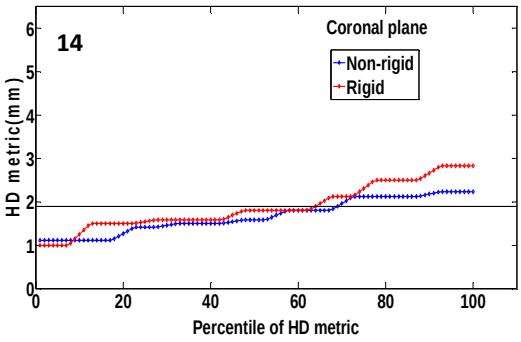
14
Coronal plane
Non-rigid
Rigid
HD metric(mm)
Percentile of HD metric

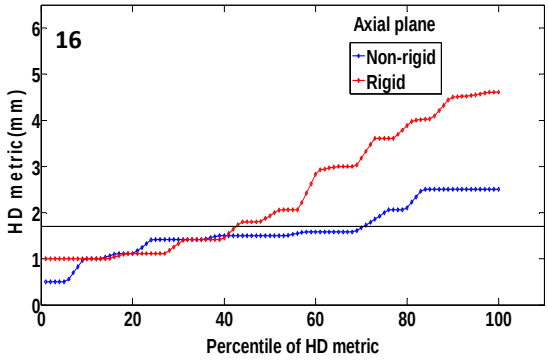
16
Axial plane
Non-rigid
Rigid
HD metric(mm)
Percentile of HD metric

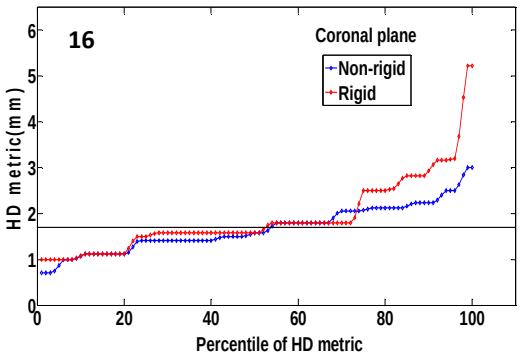
16
Coronal plane
Non-rigid
Rigid
HD metric(mm)
Percentile of HD metric

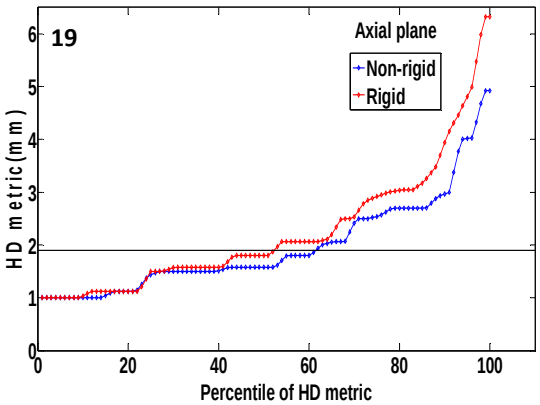
19
Axial plane
Non-rigid
Rigid
HD metric(mm)
Percentile of HD metric

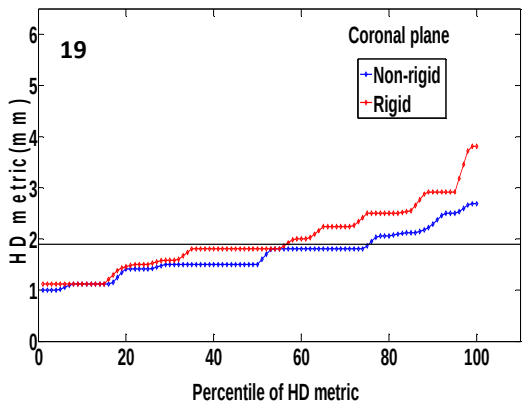
19
Coronal plane
Non-rigid
Rigid
HD metric(mm)
Percentile of HD metric

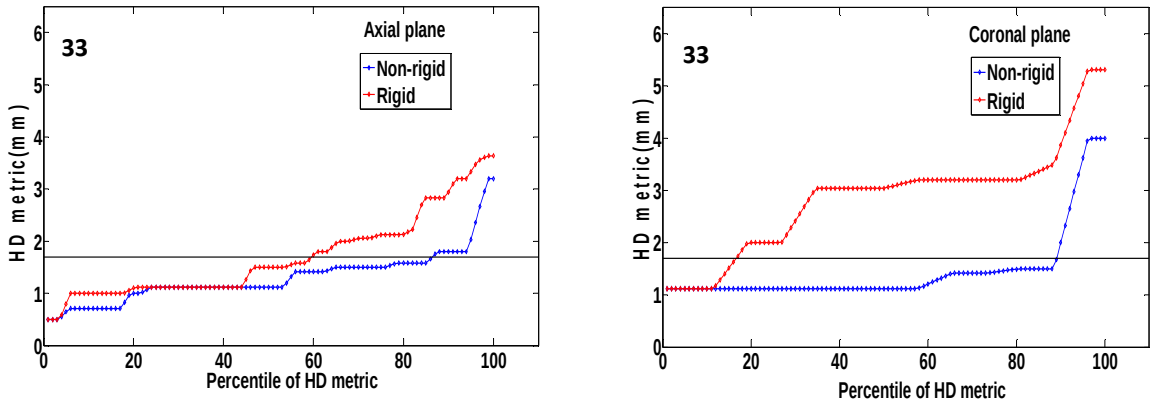

Figure 3.4: Percentile-HD metric values for axial and coronal plane (red is for Rigid registration and blue is for Biomechanical modelling based method)

100-percentile, 90-percentile and 75-percentile HD metric values for non-rigid and rigid registrations in both axial and coronal planes for 15 cases, are shown in table 3.2. 3.3 and 3.4 respectively:

Table 3.2: 100-percentile HD metric values in mm

CASE NO	Biomechanical Modelling-based non-rigid registration		Rigid Registration	
	Axial Plane	Coronal Plane	Axial Plane	Coronal Plane
CASE 01	4.12	3.64	6.10	5.00
CASE 02	3.91	3.61	6.02	2.50
CASE 03	3.50	3.50	3.50	4.03
CASE 04	2.00	3.04	5.70	6.50
CASE 05	3.53	3.50	4.00	4.30
CASE 07	3.16	2.50	6.27	4.03
CASE 08	4.30	4.30	6.10	5.50
CASE 09	3.20	3.20	4.50	6.10

CASE 10	3.61	3.50	4.61	4.53
CASE 11	4.53	4.95	5.00	6.27
CASE 12	4.12	2.83	5.41	4.24
CASE 14	4.12	2.22	5.52	2.83
CASE 16	2.50	3.00	4.61	5.22
CASE 19	4.92	2.69	6.33	3.81
CASE-28	3.20	4.00	3.64	5.32

Table 3.3: 90-percentile HD metric values in mm

CASE NO	Biomechanical Modelling-based non-rigid registration		Rigid Registration	
	Axial Plane	Coronal Plane	Axial Plane	Coronal Plane
CASE 01	3.24	3.15	4.24	3.20
CASE 02	3.54	2.67	4.93	2.50
CASE 03	2.50	2.27	2.24	2.20
CASE 04	1.80	2.66	2.94	3.81
CASE 05	2.24	3.20	3.20	3.64
CASE 07	2.83	2.24	3.65	3.54
CASE 08	3.60	3.20	4.51	3.88
CASE 09	2.12	2.23	2.69	2.77
CASE 10	3.00	3.00	2.83	3.45
CASE 11	3.78	3.50	4.06	3.91
CASE 12	2.94	2.69	3.37	3.00

CASE 14	3.62	2.20	3.80	2.66
CASE 16	2.50	2.24	4.50	2.93
CASE 19	2.97	2.29	3.94	2.92
CASE-28	1.80	2.00	2.94	3.86

Table 3.4: 75-percentile HD metric values in mm

CASE NO	Biomechanical Modelling-based non-rigid registration		Rigid Registration	
	Axial Plane	Coronal Plane	Axial Plane	Coronal Plane
CASE 01	2.55	2.41	2.92	2.12
CASE 02	2.82	2.27	3.20	2.50
CASE 03	2.11	2.12	2.07	2.06
CASE 04	1.80	1.80	2.50	2.70
CASE 05	2.08	2.62	2.30	3.16
CASE 07	1.80	1.80	2.92	2.50
CASE 08	2.83	3.00	3.00	3.20
CASE 09	1.80	2.00	2.06	2.01
CASE 10	1.46	1.94	1.75	2.15
CASE 11	3.20	3.03	3.20	3.29
CASE 12	2.15	2.22	2.00	2.82
CASE 14	2.59	2.12	2.83	2.31
CASE 16	1.99	2.08	3.61	2.50
CASE 19	2.53	1.87	2.92	2.50

CASE-28	1.50	1.44	2.12	3.20

Percentile-HD metric values and the percentage of successfully registered edges are used in tandem to assess the registration accuracy. The percentile-HD metric value curves for 14 of the 15 cases analysed, depicted clear improvement in the accuracy of the non-rigid registered pre-operative images in comparison to the rigidly registered pre-operative images. These are the cases with considerably large craniotomy-induced deformations. On the other hand, for case-03, which has low craniotomy-induced deformation, there was insignificant difference between the percentile-HD metric curves of non-rigid and rigid registrations, implying that there is insignificant improvement due to the application of biomechanical modelling-based registration.

It was observed that the 100-percentile HD metric values are larger for rigid registrations, when compared to the corresponding non-rigid registration values for each case. The only exception is case-03, which was classified as a small deformation case. Among the cases with considerably large deformation such as case-02, the 100-percentile HD metric was 2.11 mm higher for rigid registration than that of non-rigid registration in axial plane, which clearly indicates an improvement in accuracy. In coronal plane, this difference is 0.53 mm.

For the cases analysed in this study, the percentage of edges successfully registered for both biomechanical modelling-based non-rigid registration and rigid registration are summarised as follows in table 3.5. The edges with misalignment of less than two times the in-plane resolution of intraoperative image were considered successfully registered (1.7 mm or 1.9 mm, depending on the image resolution).

Table 3.5: Percentage of edges successfully registered

CASE NO	Percentage of edges successfully registered			
	Axial Slice		Coronal Slice	
	Biomechanical Modelling-based non-rigid registration	Rigid	Biomechanical Modelling-based non-rigid registration	Rigid

Case-01	51	49	51	58
Case-02	44	34	66	62
Case-03	66	70	71	69
Case-04	97	53	79	58
Case-05	69	59	38	23
Case-07	69	32	71	39
Case-08	24	22	54	56
Case-09	76	56	74	64
Case-10	88	76	75	71
Case-11	32	35	45	42
Case-12	67	66	65	29
Case-14	53	44	69	64
Case-16	71	43	52	54
Case-19	62	52	75	57
Case-33	86	60	89	16

The percentage of edges successfully registered, serves as a partial indicator of the accuracy of registration. Almost all of the 15 cases have higher percentage of successfully registered edges, when compared to that of rigid registration, except few cases where the values are close to each other.

Based on the successful improvement of neurosurgical navigation criteria mentioned in section 2.3 the responses for the fifteen cases can be summarised as follows in table 3.6:

Table 3.6: Responses based on successful improvement of neurosurgical navigation criteria due to non-rigid registration.

CASE No	Biomechanical Modelling-based non-rigid registration Successful	Rigid Registration results Successful
CASE-01	YES	NO

CASE-02	YES	NO
CASE-03	YES	YES
CASE-04	YES	NO
CASE-05	YES	NO
CASE-07	YES	NO
CASE-08	YES	NO
CASE-10	YES	NO
CASE-11	YES	NO
CASE-12	YES	NO
CASE-14	YES	NO
CASE-16	YES	NO
CASE-28	YES	NO
CASE-29	YES	NO
CASE-30	YES	NO

Based on the responses in the table 3.6, and the consideration that all the remaining small deformation cases (18 cases) experience a similar improvement in neuronavigation due to both non-rigid and rigid registrations, the P-value is **1.24692E-05** for zero difference in proportions. The P-values for different values of difference in proportions are as follows in table 3.7:

Table 3.7: P-Values at various values of difference in proportions

Delta	**P-Value**
0%	1.24692E-05

20%	0.00457
25%	0.021419568

The P-values were calculated for various values of difference in proportions or δ. For δ = 0 or equal proportions, P-value is very small in comparison to the level of significance α; whereas for difference in proportion values up to 25%, it is less than the level of significance. These values indicate strong weight of evidence favouring the rejection of H_0. Thus the hypothesis "There will be no statistically significant increase in the proportion of brain surgery patients for whom accurate data for intraoperative navigation are obtained when using our biomechanics-based non-rigid registration as compared to standard methods" can be rejected with confidence.

4. Discussion

In this study, we present a comparison between the results obtained from biomechanical modelling-based non-rigid registration to that of rigid registration. For obtaining the craniotomy-induced deformation fields, finite element meshes consisting of both hexahedral and tetrahedral elements with specialized non-linear finite element algorithms were used. The resolution of pre-operative images used in this study is low, which has made the work more challenging. The statistical analysis is strong enough to reject the hypothesis.

From the results presented in Section 3, it is apparent that the application of the intra-operative deformations predicted using patient-specific biomechanical models to warp pre-operative images ensures higher registration accuracy than that of rigid registration. Biomechanical models are very effective in neurosurgery cases, where intraoperative brain shift is large (for cases such as case-07). Another distinctive advantage of the biomechanical models is that, they do not require the intra-operative image at all to compute deformation. Only the displacement of a limited number of points on the exposed (during craniotomy) intra-operative brain surface is required.

Our experience has demonstrated that the intra-operative MRI is very useful in ensuring complete resection, particularly of low grade tumours. However, this often comes at the expense of significantly longer operating times, as well as being resource intense. The use of comprehensive biomechanical computations in the operating theatre may present a viable and economical alternative to intra-operative MRI with better accuracy. Thus the results presented in this report have the potential to significantly advance the way imaging is used to guide the resection of brain tumours.

References

BATHE, K.-J. 1996. *Finite Element Procedures*, Prentice-Hall.

BERGER, M. S., DELIGANIS, A. V., DOBBINS, J. & KELES, G. E. 2006. The effect of extent of resection on recurrence in patients with low grade cerebral hemisphere gliomas. *Cancer,* 74**,** 1784-1791.

BERGER, M. S. & ROSTOMILY, R. C. 1997. Low grade gliomas: functional mapping resection strategies, extent of resection, and outcome. *Journal of neuro-oncology,* 34**,** 85-101.

CADARSO-SUÁREZ, C. & GONZÁLEZ-MANTEIGA, W. 2007. Statistics in biomedical research. *Arbor,* 183**,** 353-361.

CANNY, J. 1986. A computational approach to edge detection. *Pattern Analysis and Machine Intelligence, IEEE Transactions on,* 679-698.

CHAKRAVARTY, M. M., SADIKOT, A. F., GERMANN, J., BERTRAND, G. & COLLINS, D. L. 2008. Towards a validation of atlas warping techniques. *Medical Image Analysis,* 12**,** 713-726.

CONNOR, R. J. 1987. Sample size for testing differences in proportions for the paired-sample design. *Biometrics,* 43**,** 207-211.

DAVIES, E., CLARKE, C. & HOPKINS, A. 1996. Malignant cerebral glioma—I: Survival, disability, and morbidity after radiotherapy. *BMj,* 313**,** 1507-1512.

FEDOROV, A., BILLET, E., PRASTAWA, M., GERIG, G., RADMANESH, A., WARFIELD, S., KIKINIS, R. & CHRISOCHOIDES, N. 2008. Evaluation of brain MRI alignment with the robust hausdorff distance measures. *Advances in Visual Computing,* 594-603.

FERRANT, M., NABAVI, A., MACQ, B., BLACK, P. M., JOLESZ, F. A., KIKINIS, R. & WARFIELD, S. K. 2002. Serial registration of intraoperative MR images of the brain. *Medical Image Analysis,* 6**,** 337-359.

GARLAPATI, R. R., JOLDES, G. R., WITTEK, A., LAM, J., WEISENFELD, N., HANS, A., WARFIELD, S. K., KIKINIS, R. & MILLER, K. 2012. Objective evaluation of accuracy of intra-operative neuroimage registration. *MICCAI 2012 workshop* NICE,France.

GOODMAN, S. N. 1999. Toward evidence-based medical statistics. 1: The P value fallacy. *Annals of internal medicine,* 130**,** 995-1004.

GROSLAND, N. M., SHIVANNA, K. H., MAGNOTTA, V. A., KALLEMEYN, N. A., DEVRIES, N. A., TADEPALLI, S. C. & LISLE, C. 2009. IA-FEMesh: An open-source, interactive, multiblock approach to anatomic finite element model development. *Computer methods and programs in biomedicine,* 94**,** 96-107.

HU, J., JIN, X., LEE, J. B., ZHANG, L., CHAUDHARY, V., GUTHIKONDA, M., YANG, K. H. & KING, A. I. 2007. Intraoperative brain shift prediction using a 3D inhomogeneous patient-specific finite element model. *Journal of neurosurgery,* 106**,** 164-169.

HUTTENLOCHER, D. P., KLANDERMAN, G. A. & RUCKLIDGE, W. J. 1993. Comparing images using the Hausdorff distance. *Pattern Analysis and Machine Intelligence, IEEE Transactions on,* 15**,** 850-863.

JOLDES, G., WITTEK, A., COUTON, M., WARFIELD, S. & MILLER, K. 2009a. Real-time prediction of brain shift using nonlinear finite element algorithms. *Medical Image Computing and Computer-Assisted Intervention–MICCAI 2009***,** 300-307.

JOLDES, G. R., WITTEK, A. & MILLER, K. 2008a. An efficient hourglass control implementation for the uniform strain hexahedron using the total Lagrangian formulation. *Communications in Numerical Methods in Engineering,* 24**,** 1315-1323.

JOLDES, G. R., WITTEK, A. & MILLER, K. 2009b. Computation of intra-operative brain shift using dynamic relaxation. *Computer methods in applied mechanics and engineering,* 198**,** 3313-3320.

JOLDES, G. R., WITTEK, A. & MILLER, K. 2009c. Non-locking tetrahedral finite element for surgical simulation. *Communications in Numerical Methods in Engineering,* 25**,** 827-836.

JOLDES, G. R., WITTEK, A. & MILLER, K. 2009d. Suite of finite element algorithms for accurate computation of soft tissue deformation for surgical simulation. *Medical image analysis,* 13**,** 912.

JOLDES, G. R., WITTEK, A. & MILLER, K. 2010. Real-time nonlinear finite element computations on GPU–Application to neurosurgical simulation. *Computer methods in applied mechanics and engineering,* 199**,** 3305-3314.

JOLDES, G. R., WITTEK, A., MILLER, K. & MORRISS, L. 2008b. Realistic and efficient brain-skull interaction model for brain shift computation. *Computational Biomechanics for Medicine III Workshop, MICCAI***,** 95-105.

JOLESZ, F. A., TALOS, I. F., SCHWARTZ, R. B., MAMATA, H., KACHER, D. F., HYNYNEN, K., MCDANNOLD, N., SAIVIRONPORN, P. & ZAO, L. 2002.

Intraoperative magnetic resonance imaging and magnetic resonance imaging-guided therapy for brain tumors. *Neuroimaging Clin N Am,* 12**,** 665-83.

KELES, G. E., LAMBORN, K. R. & BERGER, M. S. 2001. Low-grade hemispheric gliomas in adults: a critical review of extent of resection as a factor influencing outcome. *Journal of neurosurgery,* 95**,** 735-745.

LUYKEN, C., BLÜMCKE, I., FIMMERS, R., URBACH, H., ELGER, C. E., WIESTLER, O. D. & SCHRAMM, J. 2003. The Spectrum of Long-term Epilepsy–associated Tumors: Long-term Seizure and Tumor Outcome and Neurosurgical Aspects. *Epilepsia,* 44**,** 822-830.

MIGA, M. I., PAULSEN, K. D., LEMERY, J. M., EISNER, S. D., HARTOV, A., KENNEDY, F. E. & ROBERTS, D. W. 1999. Model-updated image guidance: Initial clinical experiences with gravity-induced brain deformation. *IEEE Trans. on Biomedical Engineering.,* 18**,** 866-874.

MIGA, M. I., ROBERTS, D. W., KENNEDY, F. E., PLATENIK, L. A., HARTOV, A., LUNN, K. E. & PAULSEN, K. D. 2001. Modeling of retraction and resection for intraoperative updating of images. *Neurosurgery,* 49**,** 75-85.

MILLER, K. & CHINZEI, K. 1997. Constitutive modelling of brain tissue: experiment and theory. *Journal of Biomechanics,* 30**,** 1115-1121.

MILLER, K. & CHINZEI, K. 2002. Mechanical properties of brain tissue in tension. *Journal of biomechanics,* 35**,** 483-490.

MILLER, K., JOLDES, G., LANCE, D. & WITTEK, A. 2007. Total Lagrangian explicit dynamics finite element algorithm for computing soft tissue deformation. *Communications in numerical methods in engineering,* 23**,** 121-134.

MOSTAYED, A., GARLAPATI, R. R., JOLDES, G. R., WITTEK, A., ROY, A., KIKINIS, R., WARFIELD, S. K. & MILLER, K. 2013. Biomechanical model as a registration tool for image-guided neurosurgery: evaluation against BSpline registration. *Annals of Biomedical Engineering (submitted).*

NAKAMURA, M., KONISHI, N., TSUNODA, S., NAKASE, H., TSUZUKI, T., AOKI, H., SAKITANI, H., INUI, T. & SAKAKI, T. 2000. Analysis of prognostic and survival factors related to treatment of low-grade astrocytomas in adults. *Oncology,* 58**,** 108-116.

OWEN, S. J. 2001. Hex-dominant mesh generation using 3D constrained triangulation. *Computer-Aided Design,* 33**,** 211-220.

PIEPMEIER, J., CHRISTOPHER, S., SPENCER, D., BYRNE, T., KIM, J., KNISEL, J. P., LACY, J., TSUKERMAN, L. & MAKUCH, R. 1996. Variations in the natural history and survival of patients with supratentorial low-grade astrocytomas. *Neurosurgery,* 38**,** 872-879.

REXILIUS, J., WARFIELD, S., GUTTMANN, C., WEI, X., BENSON, R., WOLFSON, L., SHENTON, M., HANDELS, H. & KIKINIS, R. A novel nonrigid registration algorithm and applications. Medical Image Computing and Computer-Assisted Intervention–MICCAI 2001, 2001. Springer, 923-931.

SCERRATI, M., ROSELLI, R., IACOANGELI, M., POMPUCCI, A. & ROSSI, G. 1996. Prognostic factors in low grade (WHO grade II) gliomas of the cerebral hemispheres: the role of surgery. *Journal of Neurology, Neurosurgery & Psychiatry,* 61**,** 291-296.

SHAFFER, J. P. 1995. Multiple hypothesis testing. *Annual review of psychology,* 46**,** 561-584.

SINKUS, R., TANTER, M., XYDEAS, T., CATHELINE, S., BERCOFF, J. & FINK, M. 2005. Viscoelastic shear properties of in vivo breast lesions measured by MR elastography. *Magnetic Resonance Imaging,* 23**,** 159-165.

SKRINJAR, O., NABAVI, A. & DUNCAN, J. A stereo-guided biomechanical model for volumetric deformation analysis. Mathematical Methods in Biomedical Image Analysis, 2001. MMBIA 2001. IEEE Workshop on, 2001. IEEE, 95-102.

SLICER, D. *3D Slicer* [Online].

THOMAS, D. G. T. & GRAHAM, D. I. 1980. *Brain tumours: scientific basis, clinical investigation and current therapy,* Butterworths.

VICECONTI, M., DAVINELLI, M., TADDEI, F. & CAPPELLO, A. 2004. Automatic generation of accurate subject-specific bone finite element models to be used in clinical studies. *Journal of biomechanics,* 37**,** 1597-1605.

VICECONTI, M. & TADDEI, F. 2003. Automatic generation of finite element meshes from computed tomography data. *Critical Reviews in Biomedical Engineering,* 31**,** 27-72.

WARFIELD, S. K., FERRANT, M., GALLEZ, X., NABAVI, A., JOLESZ, F. A. & KIKINIS, R. Real-time biomechanical simulation of volumetric brain deformation for image guided neurosurgery. SC 2000: High Performance Networking and Compting Conference, 2000 Dallas, USA. 1-16.

WARFIELD, S. K., HAKER, S. J., TALOS, I.-F., KEMPER, C. A., WEISENFELD, N., MEWES, A. U. J., GOLDBERG-ZIMRING, D., ZOU, K. H., WESTIN, C. F., WELLS, W. M., TEMPANY, C. M. C., GOLBY, A., BLACK, P. M., JOLESZ, F. A.

& KIKINIS, R. 2005. Capturing intraoperative deformations: research experience at Brigham and Womens's hospital. *Medical Image Analysis,* 9**,** 145-162.

WITTEK, A., HAWKINS, T. & MILLER, K. 2009. On the unimportance of constitutive models in computing brain deformation for image-guided surgery. *Biomechanics and modeling in mechanobiology,* 8**,** 77-84.

WITTEK, A., JOLDES, G., COUTON, M., WARFIELD, S. K. & MILLER, K. 2010. Patient-specific non-linear finite element modelling for predicting soft organ deformation in real-time; Application to non-rigid neuroimage registration. *Progress in biophysics and molecular biology,* 103**,** 292.

WITTEK, A., MILLER, K., KIKINIS, R. & WARFIELD, S. K. 2007. Patient-specific model of brain deformation: Application to medical image registration. *Journal of biomechanics,* 40**,** 919-929.

YEOH, O. 1993. Some forms of the strain energy function for rubber. *Rubber Chemistry and technology,* 66**,** 754-771.

ZHAO, C., SHI, W. & DENG, Y. 2005. A new Hausdorff distance for image matching. *Pattern Recognition Letters,* 26**,** 581-586.